Article

Optimization of the *Camellia oleifera* Fruit Harvester Engine Compartment Heat Dissipation Based on Temperature Experiments and Airflow Field Simulation

Wenfu Tong, Kai Liao *, Lijun Li, Zicheng Gao, Fei Chen and Hong Luo (ID)

Engineering Research Center for Forestry Equipment of Hunan Province, Central South University of Forestry and Technology, Changsha 410004, China; 20221100303@csuft.edu.cn (W.T.)
* Correspondence: liaokai102@csuft.edu.cn

Abstract: The *Camellia oleifera* fruit harvester, a specialized agricultural device, is engineered for efficient operation within the densely planted *C. oleifera* groves of China's undulating terrains. Its design features a notably small footprint to navigate the constrained spaces between trees. With the enhancement of the functionality and power of the harvester, the engine compartment becomes even more congested. This, while beneficial for performance, complicates heat dissipation and reduces harvesting efficiency. In this study, experiments were initially conducted to collect temperature data from the main heat-generating components and parts susceptible to high temperatures within the harvester's engine compartment. Subsequently, a 3D model was developed for numerical simulations, leading to the proposal of optimization schemes for the engine compartment's structure and the validation of these schemes' feasibility. A comparison of the experimental data, both before and after optimization, revealed a significant reduction in the surface temperatures of components within the engine compartment following optimization. As a result, the heat dissipation of the engine compartment has been greatly optimized. The harvester has demonstrated prolonged normal operation, enhancing the reliability and economy of the harvester.

Keywords: *Camellia oleifera* fruit harvester; engine compartment; heat dissipation; experimentation and simulation; structural optimization

1. Introduction

Camellia oleifera is one of the unique woody oil crops in China, and it is an important economic crop with a planting area of about 4.85 million hectares [1]. Its fruit is composed of cattails, seed shells, coats, and kernels. Usually, the seeds are physically pressed to extract Camellia oil. At present, fresh *C. oleifera* fruits are picked manually, which is costly and inefficient. If more special equipment or mechanical devices can be introduced into the practical production, it would be a better solution for the industrial development and management, as well as helping to overcome the harvesting conflict [2,3].

The *C. oleifera* fruit harvester, a specialized type of agricultural machinery, is employed in the *C. oleifera* tree groves of China's hilly regions [4]. With the national *C. oleifera* industry's development, researchers have been striving to enhance the harvester's functionality, adaptability, and cost-effectiveness [5–9]. Given the dense planting of *C. oleifera* trees, it is crucial for the harvester to maintain a compact size. Furthermore, as the harvester's functionalities expand, there is an increasing need to install sensors within the engine compartment, exacerbating the limited space issue. Additionally, to navigate the challenging terrain, it becomes necessary to progressively increase the engine's power. These developments hinder effective heat dissipation within the engine compartment. Therefore, solving the heat dissipation challenge within the engine compartment has emerged as a critical task.

The cooling system in the harvester's engine compartment is designed to draw in cold air through forced convection. However, when this cold air meets the intricate systems of components, the airflow becomes sluggish, leading to vortex formation and the creation of a complex local temperature field within the compartment. These conditions hinder the ability to maintain the overall compartment temperature within a reasonable range, causing issues such as overheating of the radiator and hydraulic systems, reduced power in the hydraulic system, diminished engine performance, and potential equipment shutdown, which seriously reduces the harvesting efficiency of the harvester. Consequently, optimizing the internal structure of the engine compartment is critically important for enhancing the harvester's reliability and cost-effectiveness.

Currently, the predominant approaches for addressing heat dissipation challenges draw upon methodologies from automotive, electrical, aerospace, and materials engineering [10–17]. Given that the harvester falls within the small agricultural vehicle category, we primarily adopt automotive engineering techniques as our foundational strategies, which are then refined and innovated upon to devise a new method tailored for heat dissipation research in small agricultural machinery. Numerical simulation, a critical technique in automotive engineering analysis, enjoys widespread application [18]. The comprehensive analysis of heat dissipation systems by Pengyu Lu et al. was conducted using a 1D/3D collaborative simulation approach, with real-time status boundary conditions and parameters facilitated through data exchange between 1D and 3D models [19]. The study by Chunhui Zhang et al. explored airflow characteristics under the engine hood, focusing on the effects of grille opening sizes and passive aerodynamic devices on cooling resistance and radiator efficiency [20].

The method of numerical simulation stands as a highly representative and classical approach, well-developed and widely utilized in exploring mechanical heat dissipation issues. However, relying exclusively on numerical simulation may lead to findings that lack solid empirical support. Consequently, an increasing number of researchers are complementing numerical simulation studies with on-site experiments to validate the rationality and effectiveness of their simulations. Jianpeng Wang et al. developed a mathematical model for automotive thermal management and conducted numerical simulations of the vehicle's flow field and temperature field. The feasibility of the simulation results was validated through an automotive thermal balance test. The results demonstrated that by sealing the cooling module, front-end module, and optimizing the deflector structure, the recirculation of hot air and the inlet air temperature of the cooling module were reduced, thereby improving the heat dissipation efficiency of the cooling module [21]. Xiaoming Xu et al. investigated the effects of different ventilation modes on the performance of electric vehicle power compartments, utilizing natural air-cooling techniques. Their findings suggest that by integrating simulation calculations with on-site collaborative analysis methods, the optimal ventilation mode can be identified both swiftly and precisely [22]. Jie Zhang proposed a multi-objective optimization method for the thermal management systems of passenger cars. By employing a 1D/3D collaborative simulation analysis alongside on-site testing, issues like excessive battery surface temperatures and engine coolant temperatures surpassing permissible levels were effectively addressed, thereby significantly reducing the vehicle's thermal risks [23]. These studies provide excellent methods for solving the heat dissipation issues in automotive engine compartments.

Compared to automobile engine compartments, the harvester's engine compartment is smaller in volume and more compact in structure. However, due to the harvester's much slower traveling speed, the effect of natural convection can be considered negligible. To better address the heat dissipation challenges in the harvester's engine compartment, this study followed a research sequence of "experimentation—identifying issues—simulation—proposing optimization solutions for identified issues—further simulation—validating the feasibility of proposed solutions—further experimentation—comparison—drawing conclusions." Initially, experiments were conducted to collect temperature data, uncovering severe heat dissipation challenges. A 3D model was then established for numerical simula-

tion, proposing optimization solutions for the internal structure of the compartment and validating the feasibility of these solutions. Finally, a comparison of the experimental data before and after optimization revealed a significant decrease in the surface temperatures of components within the compartment, thus validating the rationality and effectiveness of the improvement scheme.

2. Experiment

2.1. Experimental Setup

C. oleifera is mainly distributed in the mountainous and hilly areas of subtropical regions in southern, central, and eastern China (Figure 1). The planting area of *C. oleifera* in China accounts for 85% of the world's *C. oleifera* planting area [24].

(**a**)　　　　　　　　　　　　　　　(**b**)

Figure 1. The growth environment of *Camellia oleifera*. (**a**) Topographic features; (**b**) planting spacing.

According to long-term production experience, the recommended harvesting dates of different *C. oleifera* cultivars are the traditional Chinese solar terms, comprising Cold Dews, Frost's Descents, and Winter Begins [25]. The *C. oleifera* fruit harvester operates with a diesel engine, with the distribution of its engine compartment's internal structure shown in Figure 2.
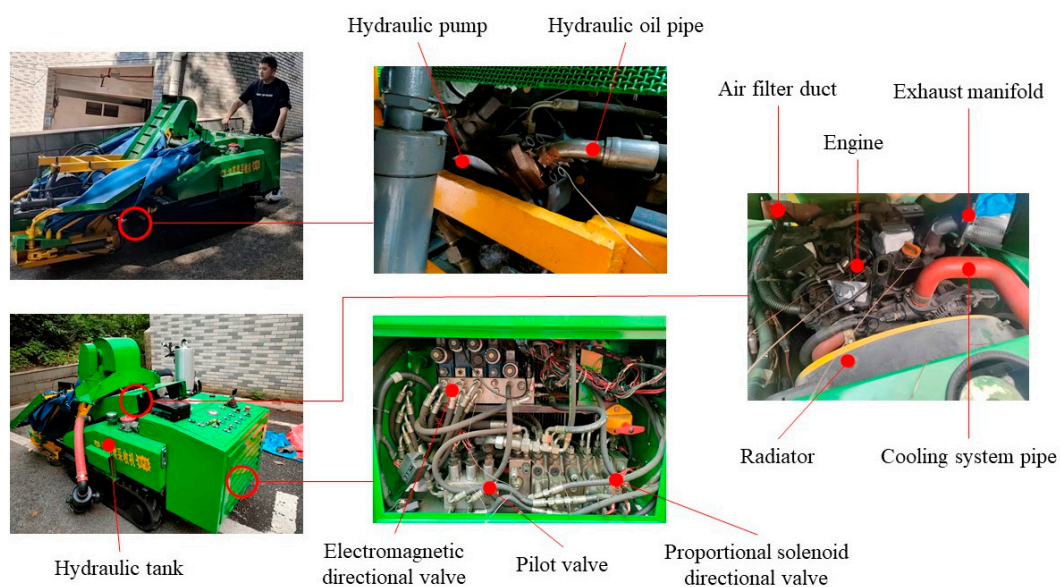

Figure 2. Internal structure schematic diagram of engine compartment.

The experiments were carried out in Shuangfeng, Hunan Province, China (27.4165° N, 112.1433° E), as detailed in Table 1, which presents the ambient parameters at the experimental site. The testing instruments required for the experiments are listed in Table 2.

Table 1. Ambient parameters of Shuangfeng.

Ambient Parameters	Shuangfeng
Weather	Sunny
Temperature	27 °C
Relative Humidity	39%
Wind Velocity	≤1.5 m/s
Slope Gradient	13.6°

Table 2. Instruments and parameters used in the experimental section.

Instruments	Manufacturer	Model Number	Range	Accuracy
Thermocouple	KAIPUSEN	K-type	−40~200 °C	±0.5%
Thermal Imager	FOTRIC	236	−20~650 °C	±2.0%
Dynamic Signal Testing Analyzer	Nanjing HOPE	HP-DS8125	/	±0.2%

In the experiment, eight temperature sensor points were established (Figure 3), all situated on the surfaces of the main heat-generating components, and those susceptible to high-temperature failure. Thermocouple temperature probes were attached to each sensor point and secured with heat-resistant tape. Subsequently, the tail end of the thermocouple was connected to the interface of the Dynamic Signal Testing Analyzer (DSTA). The temperature signal will be transmitted to the DSTA through the thermocouple, and it will form a temperature variation image. Data collection intervals were set at 1 s. Details regarding the characteristics of the sensor points are provided in Table 3.
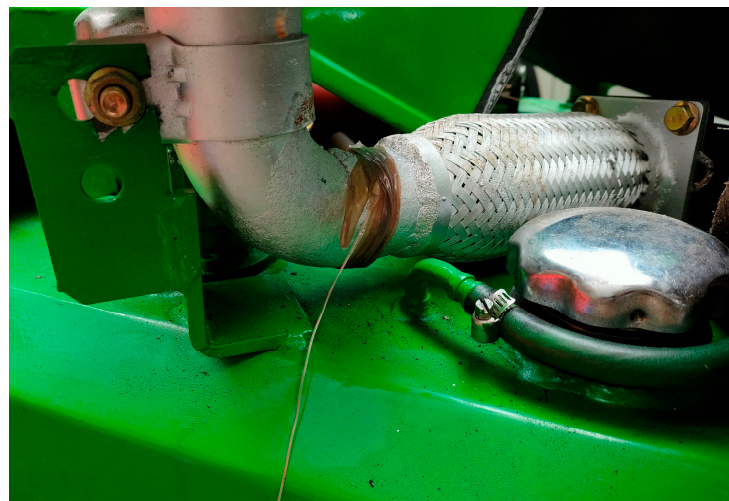
Figure 3. One of temperature sensor points (exhaust manifold).

Table 3. Temperature sensor points.

Component	Code	Point Location (Surface)
Engine	A1	Top: Near the engine compartment cover
	A2	Rear: Near the radiator
	A3	Left side: Near the valves
	A4	Right side: Near the diesel and hydraulic oil tank
Exhaust manifold	B	Base
Radiator	C	Near the coolant inlet
Hydraulic pump	D	Center
Valves	E	Top

2.2. Experimental Procedure

During the idle operation of the harvester, stable internal temperatures were achieved. Data obtained from the eight sensor points of the Dynamic Signal Testing Analyzer (DSTA) within the first 9 min of idle operation after startup are depicted in Figure 4.
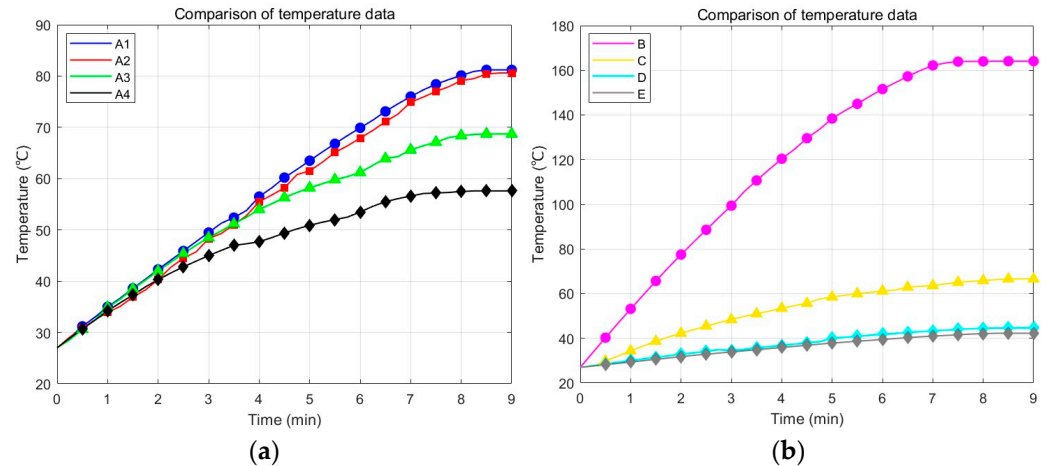

Figure 4. The temperature change graph from 0~9 min. (**a**) A1, A2, A3, A4; (**b**) B, C, D, E.

Under idle running conditions, the stable temperatures and the time required to reach these stable temperatures at each sensor point are documented in Table 4. Once the sensor points attained stable temperatures, the temperature data ceased to exhibit significant fluctuations, resulting in smooth temperature curves. Thus, it can be inferred that the temperature data from each sensor point within the harvester's engine compartment reached a basic stable state within 9 min, facilitating the commencement of subsequent experiments.

Table 4. Stable temperature and time point.

Point	Stable Temperature (°C)	Time Point (s)
A1	81.2	527
A2	80.7	535
A3	68.9	516
A4	57.6	514
B	164.2	451
C	66.7	508
D	44.7	499
E	47.5	533

The process of harvesting a single tree with the harvester includes several steps, as follows: moving to the next tree, activating the harvesting device, performing the harvest, and deactivating the harvesting device. To simulate these steps, the harvester first moves at a low speed for 20 s, then idles at a low speed for 30 s, followed by idling at a high speed for 10 s, and finally, it idles at a low speed again for 30 s. The workflow diagram of the harvester is depicted in Figure 5. During low-speed movement, the harvester's speed is approximately 0.2 m/s, and harvesting one tree takes about 1.5 min.

Since *C. oleifera* trees predominantly grow in hilly terrain areas, to mimic the road conditions encountered during the harvesting of *C. oleifera* fruits, three working conditions were established, as follows: flat ground, uphill, and downhill, as illustrated in Figure 6. After idling to achieve stable temperatures, the harvester operates on flat ground for 6 min, then transitions to working uphill for 6 min, and finally, operates downhill for another 6 min. This experiment is conducted twice. From the machine's startup to the end of the experiment, the duration is approximately 45 min. Each road condition simulates

the harvesting of four *C. oleifera* trees, resulting in a total of twenty-four *C. oleifera* trees harvested. To minimize experimental errors, the set of experiments is repeated.
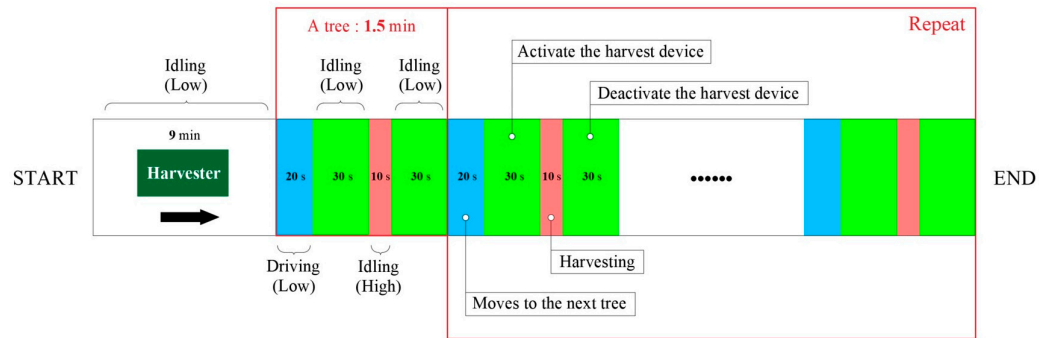

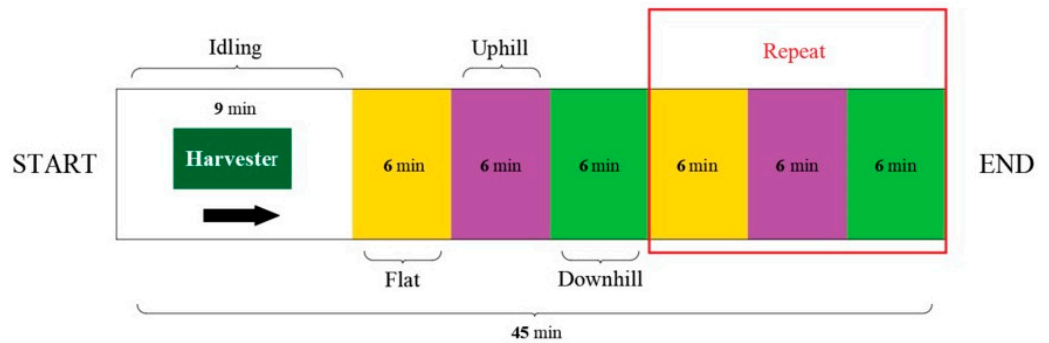
Figure 5. Harvesting workflow diagram.

Figure 6. Road conditions workflow diagram.

2.3. Experimental Result and Phenomenon

The temperature changes at the eight sensor points are depicted in Figure 7. Although thermocouple measurement is renowned for its high precision, different models of thermocouples possess limited temperature measurement ranges. Thermocouples with smaller measurement ranges exhibit relatively higher failure rates.
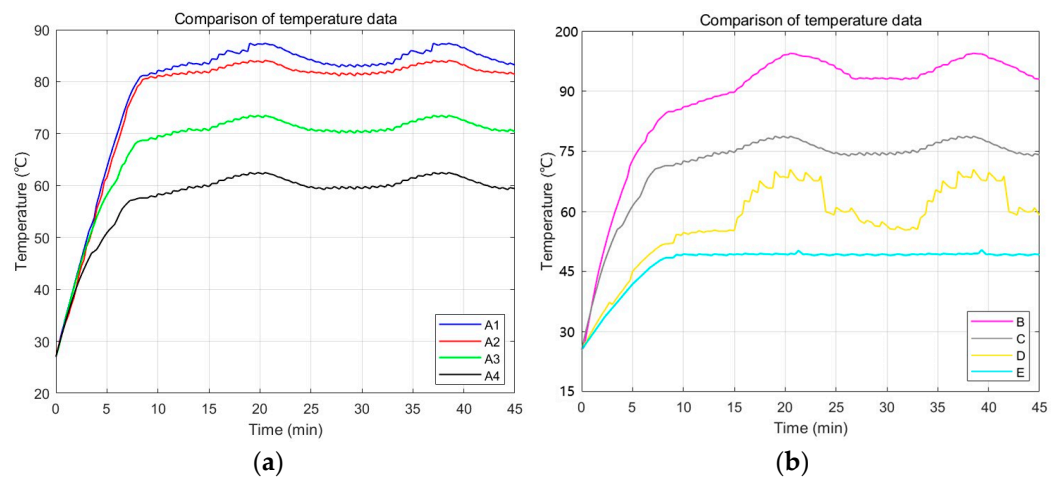

Figure 7. The temperature change graph from 0~45 min. (**a**) A1, A2, A3, A4; (**b**) B, C, D, E.

To further validate the accuracy of the thermocouple temperature measurements, temperature data collection was also performed using thermal imaging (TI) at the sensor points, as shown in Figure 8. It can be observed that there are differences in the peak temperature data measured by DSTA and TI, but the differences are not obvious.
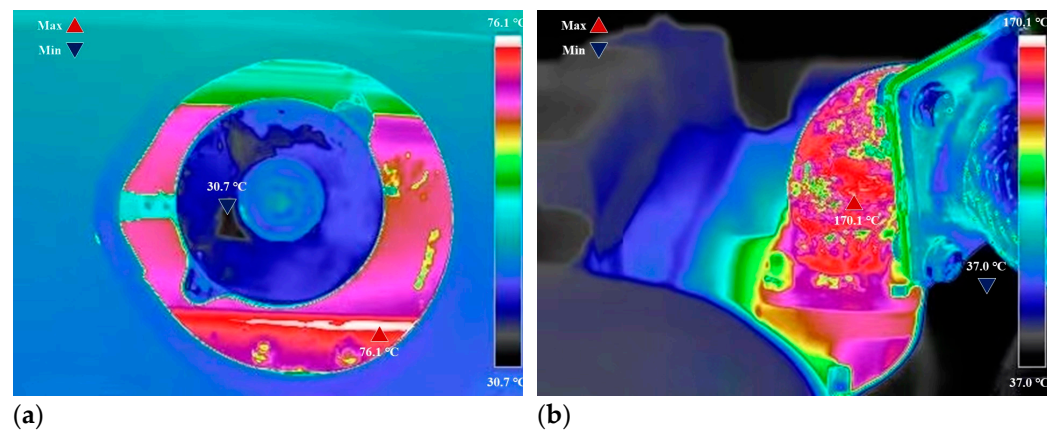
(a) **(b)**

Figure 8. Thermal imaging of partial components. (**a**) Radiator; (**b**) exhaust manifold.

At the peak temperature, the measurements obtained by the Dynamic Signal Testing Analyzer (DSTA) and TI, along with their differences, were documented in Table 5. According to the data in the table, the maximum temperature difference is 0.3 °C, and the minimum difference is 0.1 °C. The minimal discrepancy in temperature data confirms the accuracy of the temperature measurements.

Table 5. Peak temperature and time point.

Code	DSTA (°C)	TI (°C)	Difference (°C)
A1	87.4	87.2	0.2
A2	84.1	83.9	0.2
A3	73.5	73.3	0.2
A4	62.5	62.4	0.1
B	170.4	170.1	0.3
C	76.3	76.1	0.2
D	68.0	67.9	0.1
E	48.5	48.4	0.1

From the above experiments, it is observed that the temperature changes at points C and D are significant, reaching 9.7 °C and 12.3 °C, respectively. Conversely, the temperature variation at point E is relatively minor, with changes less than 1 °C. Variations at the other points fall within the range of 3 °C to 7 °C.

Approximately 20.8 and 38.5 min into the experiment, the harvester experienced a loss of hydraulic system power, characterized by a significant decrease in uphill speed and reduced steering flexibility. At the experiment's conclusion, it was observed that the coolant inlet cap of the radiator had shifted approximately 4.2° towards the loosened direction, as shown in Figure 9. Failure to promptly address the thermal management issues within the harvester's engine compartment could lead to component damage, and, in severe cases, safety incidents.

Based on the experimental data and observations, it is evident that a significant heat dissipation issue exists within the harvester's engine compartment. This necessitates identifying airflow blockage points and locations of local temperature fields through numerical simulation. The operation of the valves (E) during the experiment was unaffected by the elevated temperatures within the compartment. Therefore, in subsequent numerical simulations, the focus will be primarily on simulating airflow around the engine area, with the valves section being omitted from consideration.
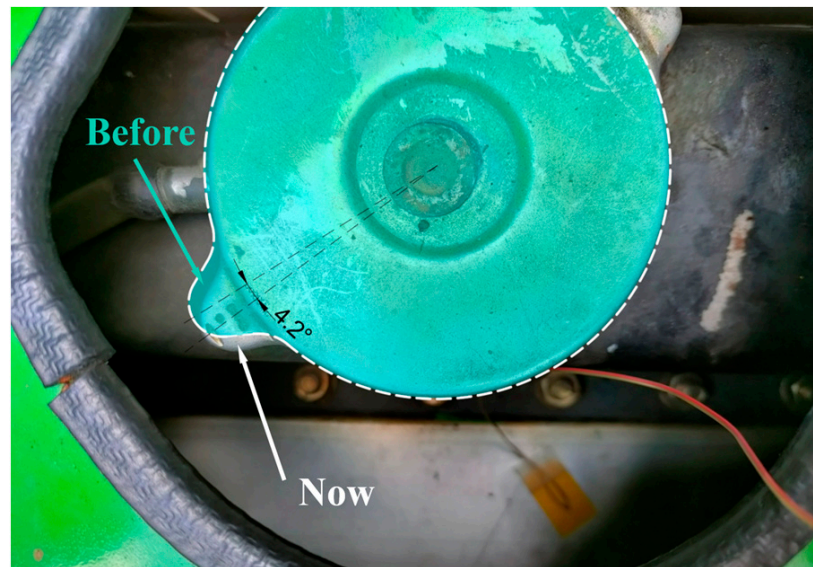
Figure 9. The position of the radiator coolant inlet cap.

3. Numerical Simulations

3.1. Turbulent Model

The choice of turbulence model significantly influences the speed of the numerical simulation process and the accuracy of the simulation results. The airflow follows the laws of mass conservation, momentum conservation, and energy conservation [26]. The air inside the engine compartment of the harvester is assumed to be incompressible, undergoing turbulent flow, in a steady state, and having uniform density. It possesses constant thermophysical properties and experiences negligible viscous dissipation. The transport equations for turbulent kinetic energy k and dissipation rate ε in the realizable $k - \varepsilon$ model are as follows:

$$\frac{\partial}{\partial t}(\rho k) + \frac{\partial}{\partial x_j}(\rho k u_j) = \frac{\partial}{\partial x_j}\left[\left(\mu + \frac{\mu_t}{\sigma_k}\right)\frac{\partial k}{\partial x_j}\right] + G_k + G_b - \rho\varepsilon - Y_M + S_k \tag{1}$$

and

$$\frac{\partial}{\partial t}(\rho\varepsilon) + \frac{\partial}{\partial x_j}(\rho\varepsilon u_j) = \frac{\partial}{\partial x_j}\left[\left(\mu + \frac{\mu_t}{\sigma_\varepsilon}\right)\frac{\partial\varepsilon}{\partial x_j}\right] + \rho C_1 S\varepsilon - \rho C_2\frac{\varepsilon^2}{k + \sqrt{\nu\varepsilon}} + C_{1\varepsilon}\frac{\varepsilon}{k}C_{3\varepsilon}G_b + S_\varepsilon \tag{2}$$

where

$$C_1 = \max\left[0.43, \frac{\eta}{\eta + 5}\right], \eta = S\frac{k}{\varepsilon}, S = \sqrt{2S_{ij}S_{ij}} \tag{3}$$

In these equations, t is time, indicating the variation of turbulent kinetic energy with respect to time. x_j represents the coordinate component of the flow field. ρ is the mass density. u_j is the velocity component of the flow field. μ is the viscosity. μ_t is the turbulent viscosity. G_k represents the generation of turbulence kinetic energy due to the mean velocity gradients. G_b represents the generation of turbulence kinetic energy due to buoyancy. Y_M represents the contribution of the fluctuating dilatation in compressible turbulence to the overall dissipation rate. S_k and S_ε are user-defined source terms. $C_{1\varepsilon}$, C_2, and $C_{3\varepsilon}$ are constants. σ_k and σ_ε are the turbulent Prandtl numbers for k and ε, respectively, and they have default values [27,28].

Compared to the standard $k - \varepsilon$ model, the realizable $k - \varepsilon$ model is characterized by a stronger analytical capability regarding streamline curvature, vortices, and rotation [29,30].

3.2. 3D Simulation Model and Mesh Generation

Due to the complexity of the arrangement of electronic circuits, pipelines, and components within the engine compartment of the harvester, directly using the original model for numerical simulation would significantly increase computation time and potentially affect the overall computational accuracy. Therefore, simplifying the model is necessary to reduce computation time and enhance the visualization of air velocity and flow trajectories. The original model was simplified using SolidWorks2022, and the simplified model is presented in Figure 10.
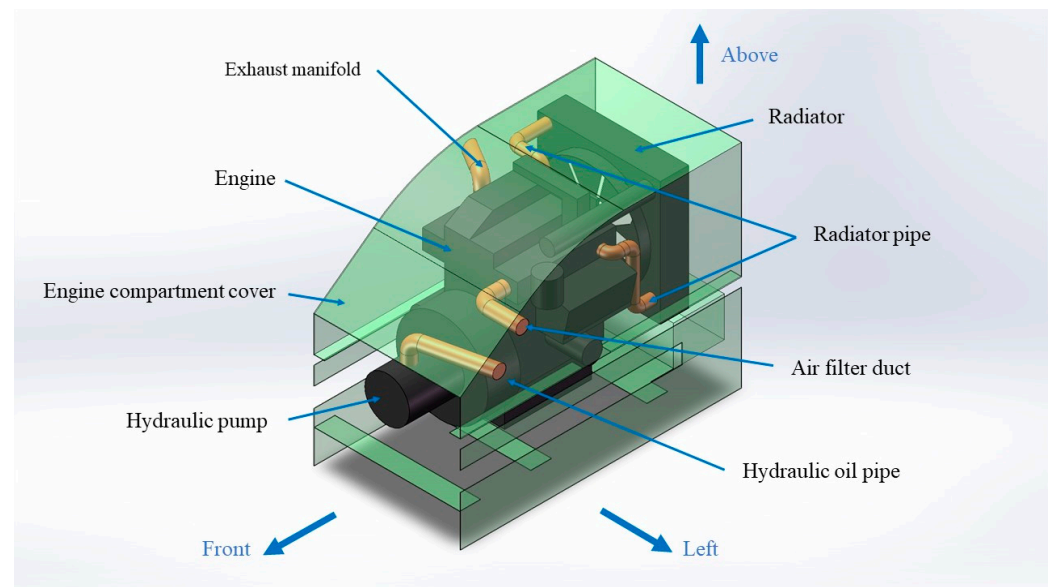

Figure 10. Simplified model.

The simplified model was employed in SpaceClaim2022R1 to create a shell, wherein each component inside the engine compartment is treated as a solid domain, and the gaps between components and other regions are considered fluid domains. The solid domain includes the engine compartment shell, engine, hydraulic pump, cooler, and large-diameter pipelines.

Mesh quality significantly influences both computational accuracy and efficiency [31]. The model employs an unstructured-tetrahedral, patch-conforming method to generate the mesh, which comprises approximately 0.25 million nodes and 1.33 million volume elements. Due to significant air velocity gradients, smaller volume elements are automatically refined locally to approximately 10 to 20 mm. The average lengths of other elements range from 30 to 60 mm. The mesh contains no negative volume elements, ensuring that the mesh quality meets the computational requirements.

3.3. Boundary Conditions and Computational Method

In the process of conducting CFD numerical simulations, it is essential to set appropriate boundary conditions to obtain solutions to the problem [32]. Accordingly, this paper provides a description of the boundary conditions involved in the CFD simulation, with the naming of boundaries as depicted in Figure 11. Assuming a fan speed of 1800 rpm, the fan's rotating area is controlled using the Moving Reference Frame (MRF) method [33], maintaining constant air density and disregarding the effects of natural convection. The fluid–structure interaction method employs the Coupled algorithm, with the simulation running for 1000 iterations.
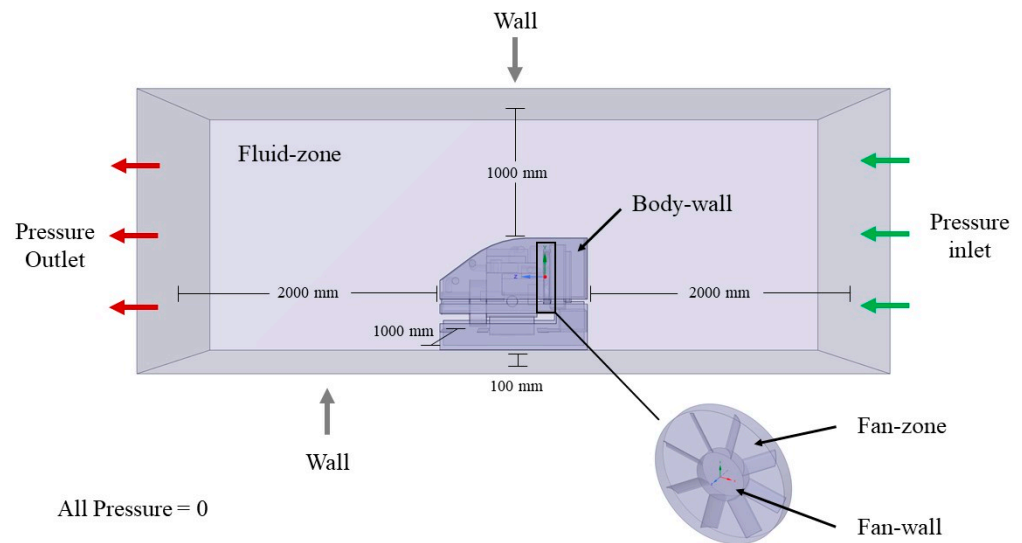
Figure 11. Name of boundary.

3.4. Result and Discussion

Convergence is achieved in the calculations around the 90th iteration. In the subsequent text, the cross-sectional positions depicted by various numerical simulation results, including the airflow velocity cloud map and air trajectory map, correspond to the position illustrated in Figure 12.
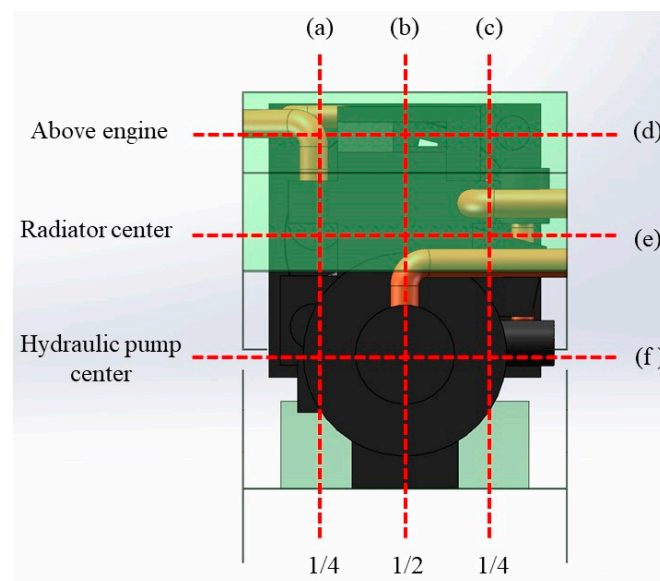

Figure 12. Cross-sectional location schematic. (**a**) 3/4 view from the left; (**b**) 1/2 view from the left; (**c**) 1/4 view from the left; (**d**) Top view of the engine above; (**e**) Top view of the radiator center; (**f**) Top view of the hydraulic pump center.

According to the airflow velocity cloud map (Figure 13), the airflow velocity inside the engine compartment decreases extremely rapidly, and the airflow passage is noticeably obstructed. When the high-speed airflow generated by the fan encounters the surfaces of complex components, it is compelled to change direction, leading to a significant reduction in speed and dispersion in direction. Simultaneously, the space within the engine compartment is extremely limited, and the airflow exhaust channel is narrow. These factors contribute significantly to the relatively obvious attenuation of wind speed.
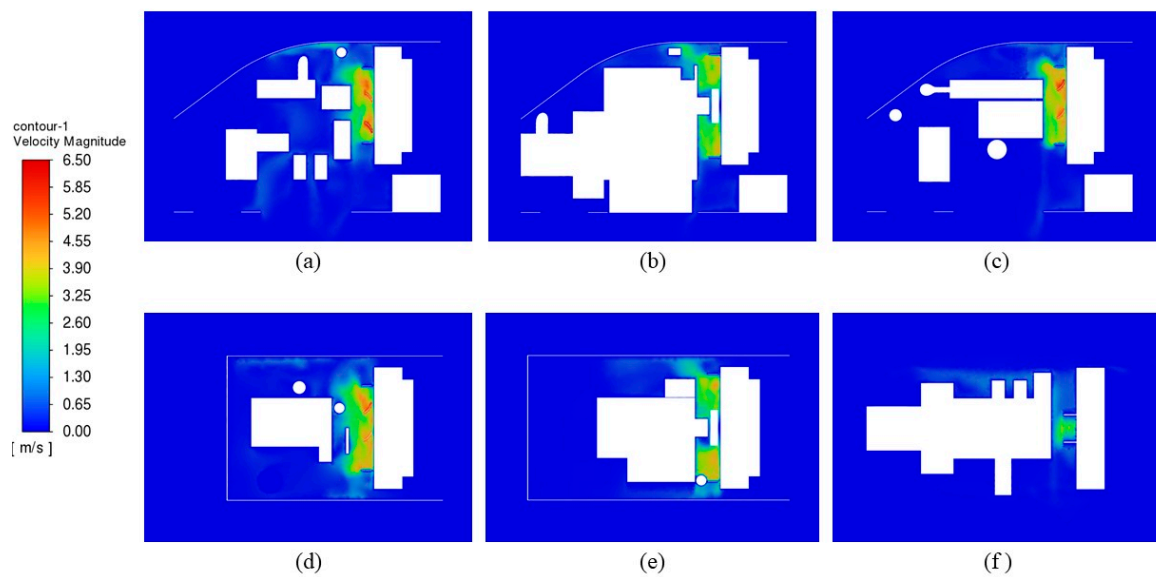
Figure 13. Airflow velocity profile cloud map. (**a**) 3/4 view from the left; (**b**) 1/2 view from the left; (**c**) 1/4 view from the left; (**d**) Top view of the engine above; (**e**) Top view of the radiator center; (**f**) Top view of the hydraulic pump center.

According to the airflow trajectory line (Figure 14), the gas trajectory lines are rather sparse. The quantity of high-temperature air exhaust channels is limited and not prominent. A considerable number of eddies are formed within the engine compartment, and the area of these eddies is relatively large. This condition is unfavorable for the proper heat dissipation of the engine compartment of the harvester.
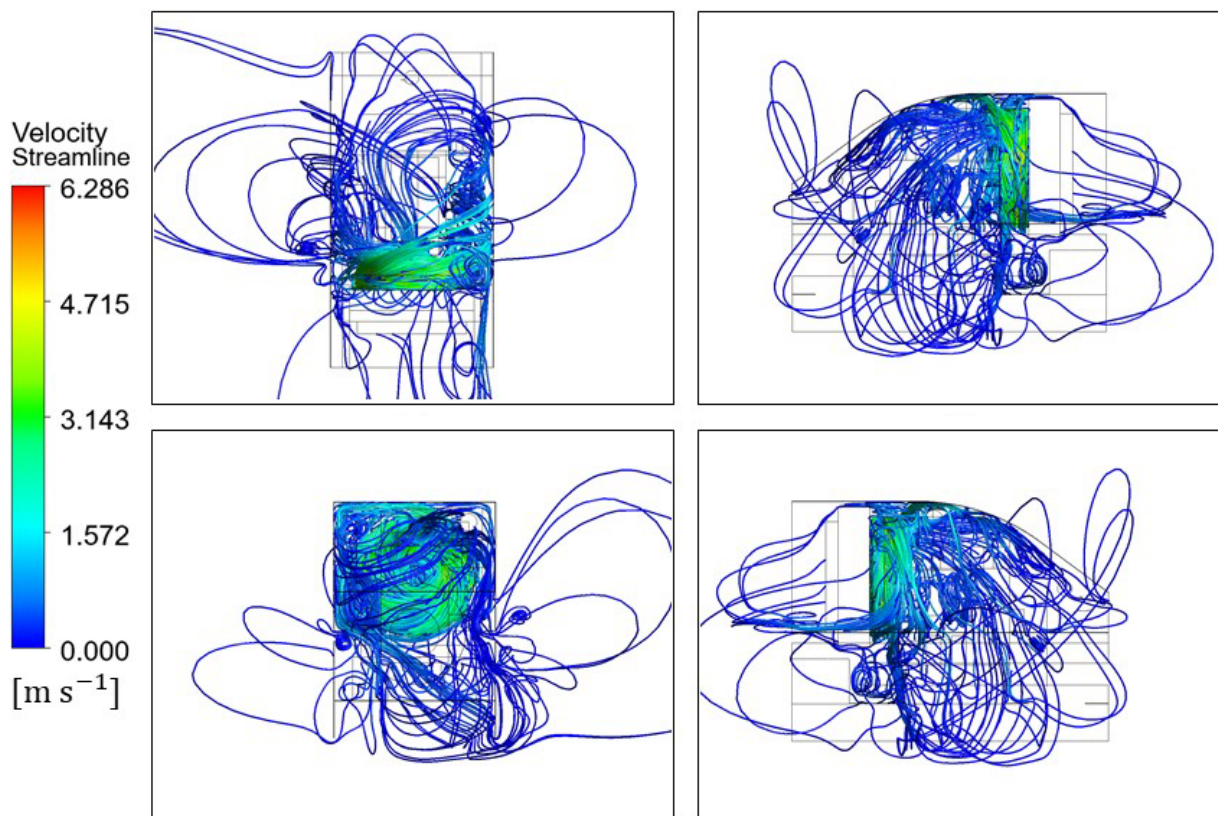

Figure 14. Airflow trajectory line.

This condition easily facilitates the formation of a heat cycle, thereby causing difficulty in heat dissipation. A preliminary assumption suggests that the blockage point of the thermal channel may be located at the top of the engine, the exhaust manifold, and the right side of the engine. It is now necessary to optimize the internal structure of the engine compartment based on this 3D model. Subsequent numerical simulations will be conducted to determine the location of the blockage point in the thermal channel, and to validate the feasibility of the optimization scheme.

4. Optimization

4.1. Structural Modification

The optimized simplified model is depicted in Figure 15. The adjustment scheme is formulated in accordance with the results of numerical simulation. Its purpose is to eliminate the obstacle points in the air-flow channels within the engine compartment of the harvester, to increase the number of channels for discharging high-temperature air, and to substantially reduce the quantity and area of eddies. The optimization plan includes the utilization of a new engine, lowering the entire engine by 85 mm and moving it backward by 230 mm, trimming the front end of the engine compartment cover by 288 mm, relocating the air filter pipe to the rear of the engine, arranging the exhaust manifold forward with the exhaust outlet positioned beneath the machine, and placing the hydraulic oil tank on the same side as the diesel tank. Upon conducting the weight distribution and balance test of the entire vehicle, it is determined that the adjustment of the overall weight and center of gravity of the harvester will not exert an unfavorable impact on the maneuverability of the harvester.
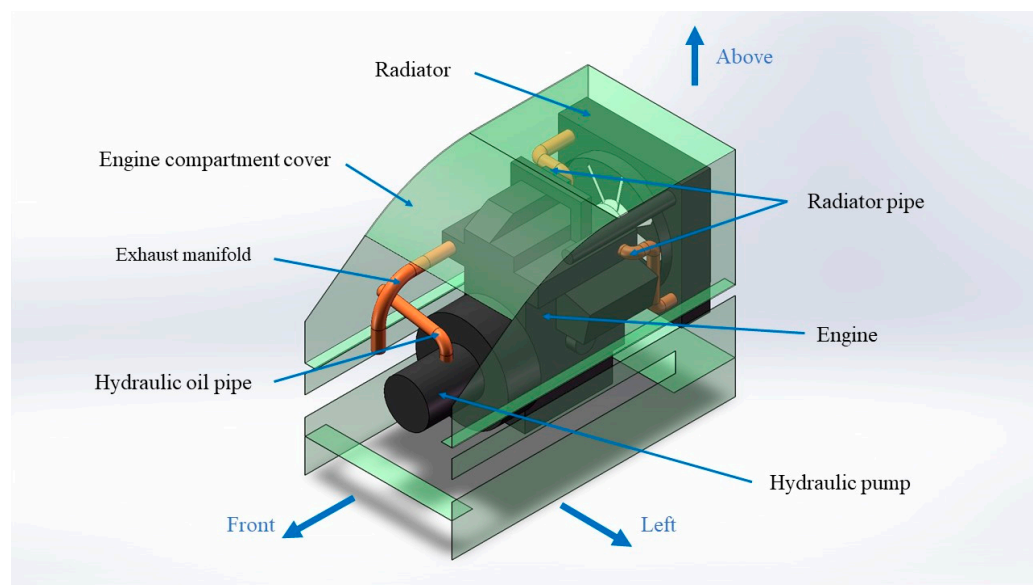

Figure 15. Optimized simplified model.

4.2. Verify the Optimization Scheme

The procedures for establishing the grid and boundary conditions are fully aligned with the methods outlined in Sections 3.2 to 3.3. The cross-sectional location is the same as that shown in Figure 12. Based on the results of numerical simulation, on the side within the engine compartment, the deceleration trend of air-flow velocity is mitigated. The significant increase in the flow velocity of air downward to the harvester can be regarded as the opening of the downward flow channel (Figure 16).
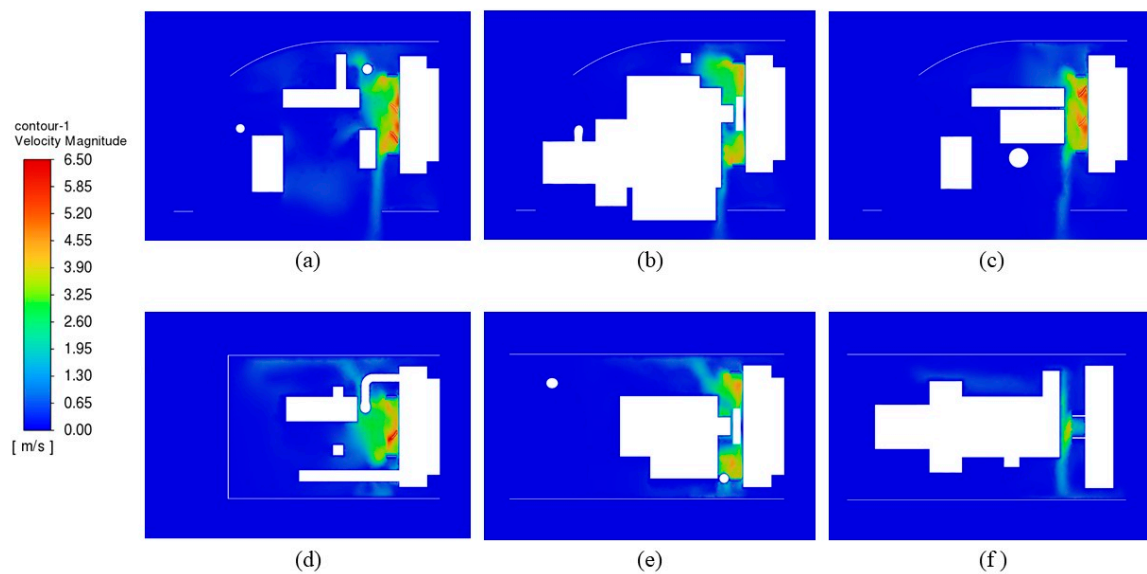
Figure 16. Optimized air-flow velocity profile cloud map. (**a**) 3/4 view from the left; (**b**) 1/2 view from the left; (**c**) 1/4 view from the left; (**d**) Top view of the engine above; (**e**) Top view of the radiator center; (**f**) Top view of the hydraulic pump center.

In accordance with the airflow trajectory lines (Figure 17), the gas trajectory lines are more concentrated compared to before optimization. The quantity of high-temperature exhaust channels is augmented. The number of eddies within the engine compartment is notably reduced. As depicted by the air-flow velocity map, the downward flow channel has been opened. Nevertheless, the small-area eddies generated upon contact with the ground cannot be avoided. The results demonstrate that the optimization scheme is feasible.
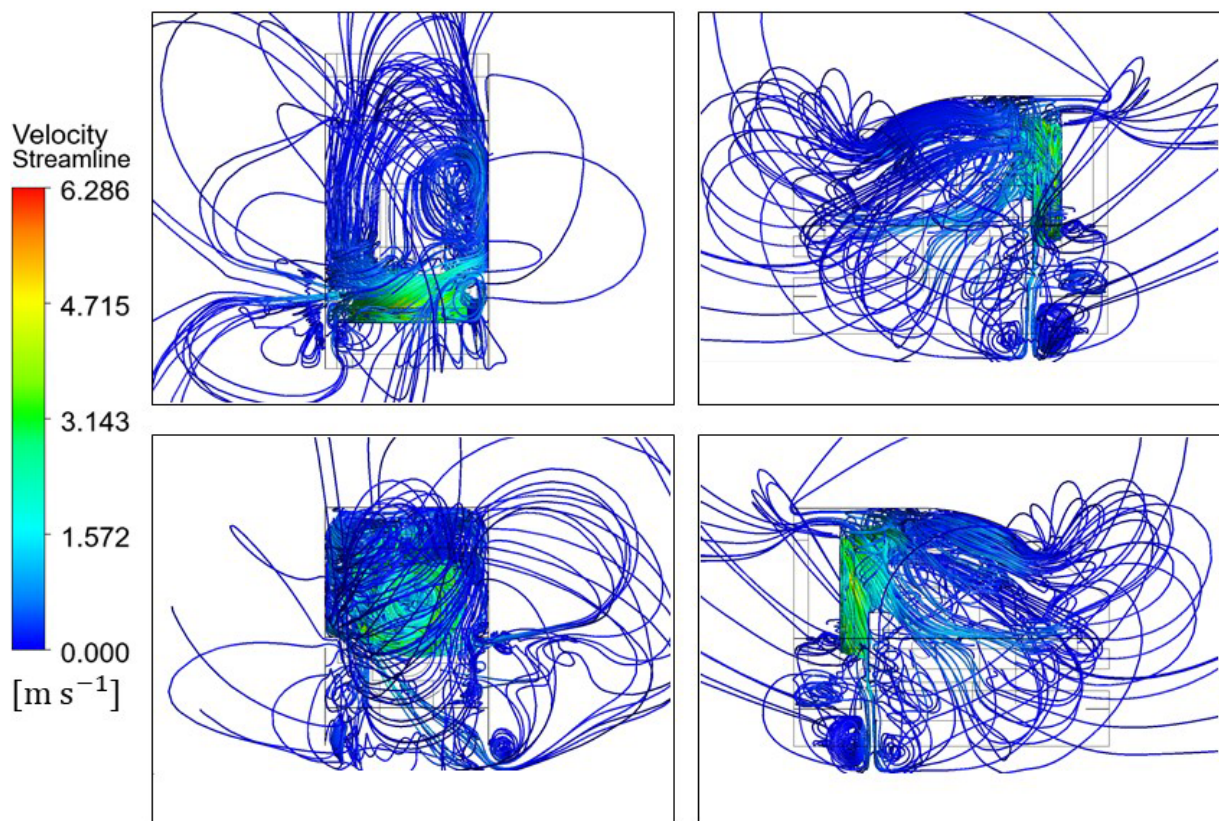

Figure 17. Optimized airflow trajectory line.

Table 6 documents the positions of airflow blockages and the state variations before and after optimization. Through the comparison of numerical simulation results prior to and following optimization, it can be preliminarily inferred that the optimization scheme for the internal structure of the harvester engine compartment is both feasible and rational. Subsequently, this optimization scheme will be implemented in the harvester and subjected to verification. The verification experiment will be carried out to determine whether this scheme can effectively optimize the heat dissipation of the harvester, and whether it is beneficial for the long-term normal operation of the harvester.

Table 6. The comparison of effects before and after optimization.

Location	Before	After	How
Engine top	Blocking	Unobstructed	Solved
Engine right side	Numerous small vortices	No vortices	Solved
Exhaust manifold	Velocity–slow	Velocity–increasing	Solved

5. Verification

5.1. Experimental Setup and Procedure

The experiment was conducted in Fenyi, Jiangxi Province, China (27.7474° N, 114.6529° E). The environmental parameters of the location are detailed in Table 7. Due to modifications in the internal structure of the engine compartment, adjustments were made to the quantity and placement of temperature sensor points, as outlined in Table 8.

Table 7. Ambient parameters of Fenyi.

Ambient Parameters	Fenyi
Weather	Sunny
Temperature	25 °C
Relative Humidity	36%
Wind Velocity	≤1.5 m/s
Slope Gradient	14.5°

Table 8. Newly set temperature sensing point.

Component	Code	Point Location (Surface)
Engine	F1	Top: Near the engine compartment cover
	F2	Right side: Near the diesel and hydraulic oil tank
Valves	G	Near the engine
Exhaust manifold	H	Base
Radiator	I	Near the coolant inlet cap
Hydraulic pump	J	Top

5.2. Experimental Result

During the experimentation process, the temperature variations at six sensor points over the period from 0 to 45 min are depicted in Figure 18. It can be readily observed that the fluctuation amplitudes of each temperature change curve are reduced, and the values are also diminished.

As in Section 2.3, temperature verification at the sensor points was conducted using thermal imaging (TI), as shown in Figure 19.

At peak temperatures, the temperatures measured by the Dynamic Signal Testing Analyzer (DSTA), those recorded by the TI, and the differences between them are detailed in Table 9. According to the data in the table, the maximum temperature difference is 0.2 °C, while the minimum is 0 °C, indicating that the data are largely consistent. Following the conclusion of the experiment, the machine operated normally, without any observed anomalies.
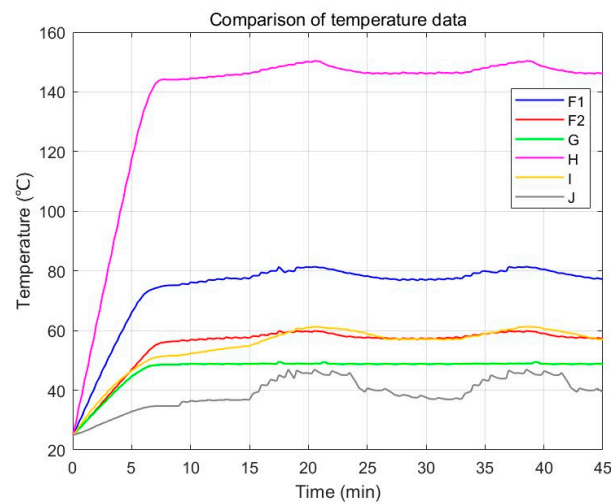
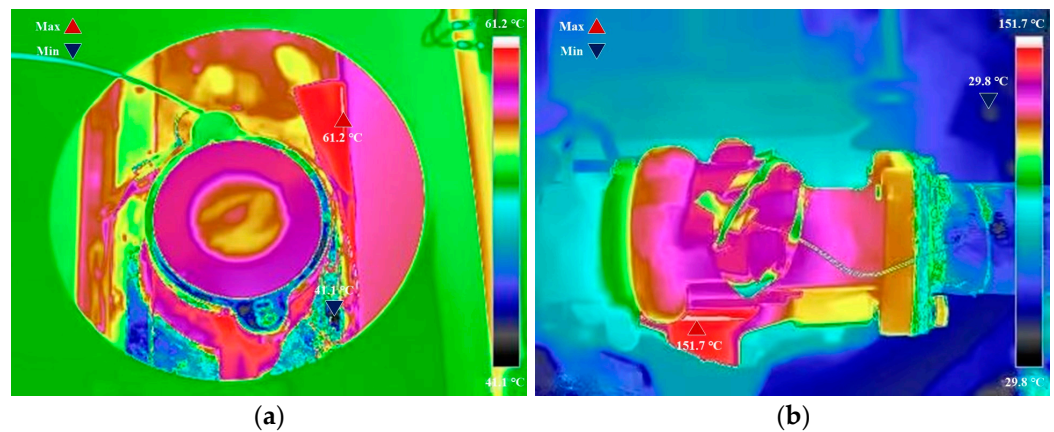**Figure 18.** The temperature change graph from 0~45 min.

Figure 19. Optimized Thermal imaging of partial components. (**a**) Radiator; (**b**) exhaust manifold.

Table 9. Comparison of peak temperature data.

Code	DSTA (°C)	TI (°C)	Difference (°C)
F1	81.7	81.6	0.1
F2	59.9	59.8	0.1
G	49.6	49.6	0
H	151.9	151.7	0.2
I	61.3	61.2	0.1
J	47.7	47.7	0

6. Comparison of Experimental Results

After the experiment, a comparison was made between the maximum temperatures and the time required to reach these maximum temperatures for the main heating components and components vulnerable to high temperatures inside the engine compartments of the two harvesters, as depicted in Figure 20. The experimental results indicate that, compared to the original harvester, the optimized harvester has experienced a significant decrease in both the maximum temperatures of the main heating components and high-temperature vulnerable components within the engine compartment, as well as the time taken to reach these maximum temperatures. Specifically, the surface temperature at the top of the engine decreased by 5.7 °C, with a reduction in time by 92 s; the surface temperature at the right side of the engine decreased by 2.6 °C, with a reduction in time by 94 s; the surface temperature of the exhaust manifold decreased by 18.5 °C, with a reduction in time

by 179 s; the surface temperature of the radiator decreased by 15.0 °C, with a reduction in time by 79 s; and the surface temperature of the hydraulic pump decreased by 6.7 °C, with a reduction in time by 123 s. The valve group, after adjusting its position, is basically not affected by temperature changes.
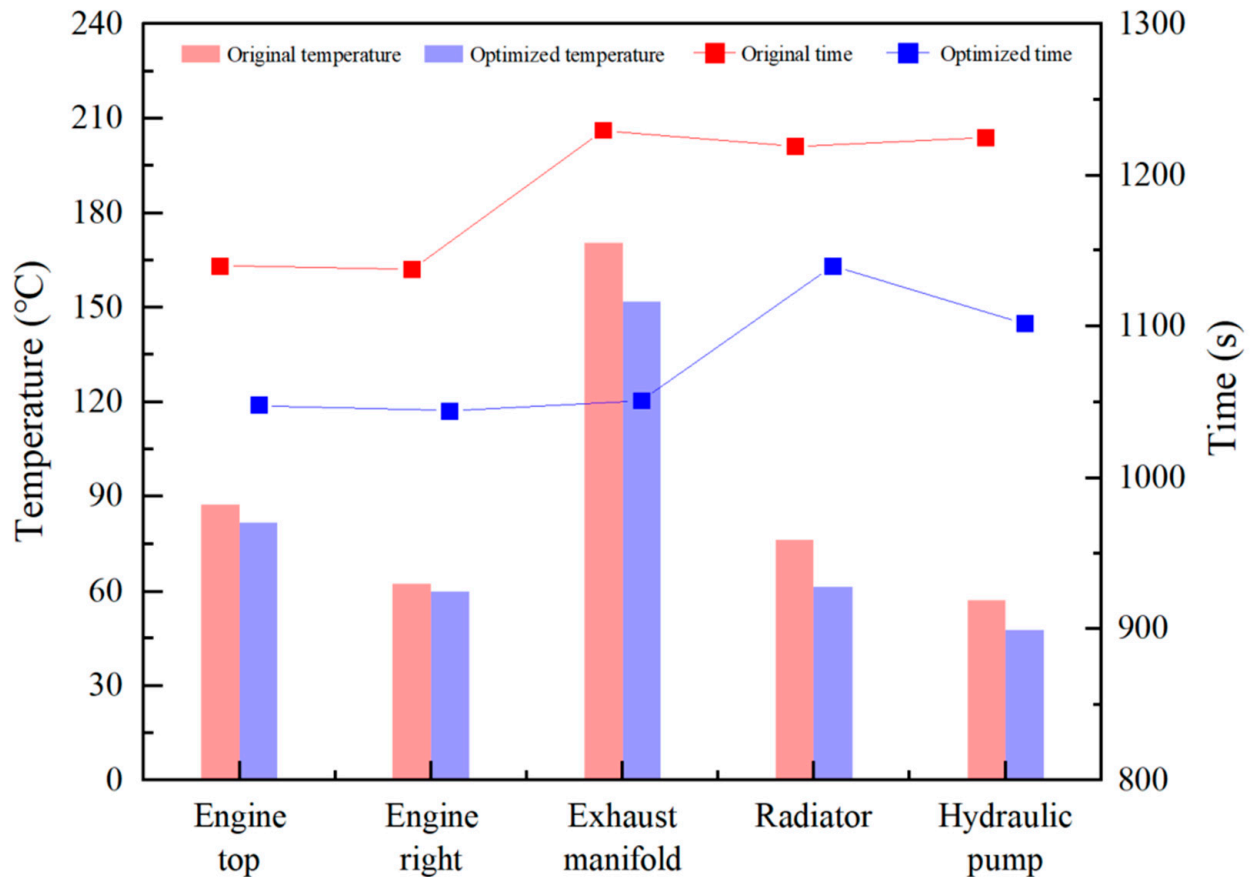

Figure 20. Maximum temperatures and time points of first attainment of maximum temperature.

Following the experiment, the *C. oleifera* fruit harvester was made to continue to perform harvesting operations for as long as four hours at the experimental site. The harvester was found to be in a normal working state, and there was no occurrence of phenomena such as power loss of the hydraulic system, significant reduction in slope speed, diminished steering flexibility, and offset of the cooler inlet cover, as mentioned previously. Hence, it can be concluded that the experimental design is rational, and the optimization scheme is effective.

7. Conclusions

Prior to structural optimization, the *C. oleifera* fruit harvester would be subject to phenomena such as power loss of the hydraulic system, significant reduction in slope speed, diminished steering flexibility, and offset of the cooler inlet cover, as mentioned previously after prolonged operation. Through experiments and numerical simulations conducted on the harvester engine compartment, it was observed that, prior to optimization, the airflow channels within the harvester engine compartment were blocked, rendering it difficult for high-temperature air to be discharged outside the compartment. This had an adverse impact on components that are prone to failure when exposed to high temperatures, resulting in decreased harvesting efficiency and safety risks that required immediate attention. This study focuses on employing a collaborative approach of experiments and numerical simulations. Firstly, the temperature field and airflow field of the harvester engine compartment are analyzed. Then, the internal structure of the engine compartment

is optimized. Finally, the rationality of the experimental design and the effectiveness of the optimization scheme are verified, thereby resolving the problem of difficult heat dissipation within the harvester engine compartment and enabling the harvester to operate normally for an extended period. The following conclusions can be drawn:

1. A method for resolving the heat dissipation issue in small agricultural machinery was employed, characterized by its straightforward principle and ease of implementation. This method offers guidance for managing thermal issues in small agricultural machinery.

2. The highest surface temperatures of various components within the harvester's compartment are located at the exhaust manifold. The engine acts as the primary heat source, while the effectiveness of the radiator and hydraulic pump varies significantly with temperature fluctuations.

3. Through experimentation on the pre-improved harvester, it was observed that the heat channels within the engine compartment were significantly obstructed, leading to occurrences such as the displacement of the coolant inlet cap of the radiator and insufficient pressure from the hydraulic pump (due to decreased viscosity of the hydraulic oil caused by heating). Numerical simulations can effectively and accurately identify the blocked points in the heat channels and provide crucial references for structural optimization.

4. Following the experiments, the improved harvester was relocated to hilly terrain and operated continuously for four hours without any issues, indicating that the heat dissipation problem within the engine compartment was effectively resolved after structural optimization.

References

1. Wu, Z.; Li, L.; Zhao, Q.; Guo, X.; Li, J. Design and Research of a Harvesting Actuator for *Camellia oleifera* Flowers during the Budding Period. *Agriculture* **2022**, *12*, 1698. [CrossRef]
2. Liu, Y.; Wang, H.; Liu, Y.; Luo, Y.; Li, H.; Chen, H.; Liao, K.; Li, L. A trunk detection method for *Camellia oleifera* fruit harvesting robot based on improved YOLOv7. *Forests* **2023**, *14*, 1453. [CrossRef]
3. Wu, D.; Yang, J.; Liu, Y.; Zhao, E.; Liu, L.; Cao, C. Research progress and trend of camellia fruit picking equipment in China. *J. Chin. Agric. Mech.* **2022**, *43*, 186–192.
4. Wu, D.; Ding, D.; Cui, B.; Jiang, S.; Zhao, E.; Liu, Y.; Cao, C. Design and experiment of vibration plate type camellia fruit picking machine. *Int. J. Agric. Biol. Eng.* **2022**, *15*, 130–138. [CrossRef]

5. Du, X.; Shen, T.; Chen, K.; Zhang, G.; Yao, X.; Chen, J.; Cao, Y. Simulation study and field experiments on the optimal canopy shaking action for harvesting *Camellia oleifera* fruits. *J. Agric. Eng.* **2022**, *53*, 1245. [CrossRef]
6. Wu, D.; Zhao, E.; Jiang, S.; Da, D.; Liu, Y. Influence of excitation position on mechanized picking effect of *Camellia oleifera*. *Eng. Agrícola* **2022**, *42*, e20220040. [CrossRef]
7. Wu, D.; Zhao, E.; Fang, D.; Liu, Y.; Wang, S.; Wu, C.; Guo, F. Experiment and analysis of mechanized picking of *Camellia oleifera* fruit based on energy utilization rate. *INMATEH Agric. Eng.* **2023**, *69*, 177–184. [CrossRef]
8. Kang, D.; Fan, Y.; Ma, F.; Peng, S.; Chen, Z. Design of Fruit Picking Machine for *Camellia oleifera*. *Int. Core J. Eng.* **2021**, *7*, 7–11.
9. Kang, D.; Fan, Y.; Chen, Z.; Ma, F.; Peng, S.; Wang, Y. *Camellia oleifera* Harvester Based on Model Processing. *J. Phys. Conf. Ser.* **2021**, *2066*, 012112. [CrossRef]
10. Marshall, G.J.; Mahony, C.P.; Rhodes, M.J.; Daniewicz, S.R.; Tsolas, N.; Thompson, S.M. Thermal management of vehicle cabins, external surfaces, and onboard electronics: An overview. *Engineering* **2019**, *5*, 954–969. [CrossRef]
11. Previati, G.; Mastinu, G.; Gobbi, M. Thermal management of electrified vehicles—A review. *Energies* **2022**, *15*, 1326. [CrossRef]
12. Sevinchan, E.; Dincer, I.; Lang, H. A review on thermal management methods for robots. *Appl. Therm. Eng.* **2018**, *140*, 799–813. [CrossRef]
13. Wang, Q.; Wu, Y.; Niu, S.; Zhao, X. Advances in thermal management technologies of electrical machines. *Energies* **2022**, *15*, 3249. [CrossRef]
14. Jiang, F.; Zhao, S.; Wang, L.; Yu, S.; Guan, H.; Liu, J. Energy Harvesting and Thermal Management System in Aerospace. *Front. Mater.* **2022**, *9*, 907858. [CrossRef]
15. Doty, J.; Yerkes, K.; Byrd, L.; Murthy, J.; Alleyne, A.; Wolff, M.; Heister, S.; Fisher, T.S. Dynamic thermal management for aerospace technology: Review and outlook. *J. Thermophys. Heat Transf.* **2017**, *31*, 86–98. [CrossRef]
16. Jung, Y.; Kim, M.; Kim, T.; Ahn, J.; Lee, J.; Ko, S.H. Functional materials and innovative strategies for wearable thermal management applications. *Nano-Micro Lett.* **2023**, *15*, 160. [CrossRef]
17. Yang, S.; Lin, J.; Zhang, Z.; Zhang, C.; Zheng, X.; Xie, W.; Wang, L.; Chen, S.; Liu, X. Advanced engineering materials for enhancing thermal management and thermal safety of lithium-ion batteries: A review. *Front. Energy Res.* **2022**, *10*, 949760. [CrossRef]
18. Wang, Y.; Gao, Q.; Zhang, T.; Wang, G.; Jiang, Z.; Li, Y. Advances in integrated vehicle thermal management and numerical simulation. *Energies* **2017**, *10*, 1636. [CrossRef]
19. Lu, P.; Gao, Q.; Wang, Y. The simulation methods based on 1D/3D collaborative computing for the vehicle integrated thermal management. *Appl. Therm. Eng.* **2016**, *104*, 42–53.
20. Zhang, C.; Uddin, M.; Robinson, A.C.; Foster, L. Full vehicle CFD investigations on the influence of front-end configuration on radiator performance and cooling drag. *Appl. Therm. Eng.* **2018**, *130*, 1328–1340.
21. Wang, J.; Yang, T.; Zhang, Z. Numerical Simulation and Experimental Research on Engine Room Heat Dissipation Performance of a Hybrid Car. In Proceedings of the IOP Conference Series: Materials Science and Engineering, Virtual, 1 October 2021; IOP Publishing: Bristol, UK, 2021; Volume 1194, p. 012005.
22. Xu, X.; Fu, J.; Hu, D.; Li, R. Heat dissipation performance of electric vehicle cabin under natural wind cooling. *Adv. Mech. Eng.* **2018**, *10*, 1687814018803819. [CrossRef]
23. Zhang, J.; Wang, Q.; Shu, C.-M.; Zhang, M.; Lin, J. A multi-objective optimization method for under-the-hood thermal management of vehicles. *Appl. Therm. Eng.* **2021**, *192*, 116818. [CrossRef]
24. Yan, F.; Li, X.; Huang, G.; Li, X. *Camellia oleifera* fresh fruit harvesting in China. In Proceedings of the 2020 5th International Conference on Mechanical, Control and Computer Engineering (ICMCCE), Harbin, China, 25–27 December 2020; IEEE: New York, NY, USA, 2020.
25. Wang, J.; Gao, X.; Liu, M.; Li, J.; Yang, H.; Wang, Z.; Yang, L. *Camellia* oil trait and DIA quantitative proteomics analyses reveal the impact of harvesting time on the oil content and quality of the late-maturing cultivar *C. oleifera* 'Huaxin'. *Food Qual. Saf.* **2022**, *6*, fyac055. [CrossRef]
26. Khalaji, M.N.; Koca, A.; Kotcioğlu, İ. Investigation of numerical analysis velocity contours k-ε model of RNG, standard and realizable turbulence for different geometries. *Int. J. Innov. Res. Rev.* **2019**, *3*, 29–34.
27. Launder, B.E.; Spalding, D.B. The Numerical Computation of Turbulent Flow. *Comput. Methods Appl. Mech. Eng.* **1974**, *3*, 269–289. [CrossRef]
28. Kim, S.-E.; Choudhury, D.; Patel, B. Computations of complex turbulent flows using the commercial code FLUENT. In *Modeling Complex Turbulent Flows*; Springer: Dordrecht, The Netherlands, 1999; pp. 259–276.
29. Shih, T.-H.; Liou, W.W.; Shabbir, A.; Yang, Z.; Zhu, J. A New k—ε Eddy-Viscosity Model for High Reynolds Number Turbulent Flows—Model Development and Validation. *Comput. Fluids* **1995**, *24*, 227–238. [CrossRef]
30. Shaheed, R.; Mohammadian, A.; Gildeh, H.K. A comparison of standard k-ε and realizable k-ε turbulence models in curved and confluent channels. *Environ. Fluid Mech.* **2019**, *19*, 543–568. [CrossRef]
31. Schneider, T.; Hu, Y.; Dumas, J.; Gao, X.; Panozzo, D.; Zorin, D. Decoupling simulation accuracy from mesh quality. *ACM Trans. Graph.* **2018**. [CrossRef]

32. Bumrungthaichaichan, E. How can the appropriate near-wall grid size for gas cyclone CFD simulation be estimated? *Powder Technol.* **2022**, *396*, 327–344. [CrossRef]
33. Mehravaran, M.; Zhang, Y. Optimizing the Geometry of Fan-Shroud Assembly Using CFD. No. 2015-01-1336. *SAE Tech. Paper.* 2015. Available online: https://www.sae.org/publications/technical-papers/content/2015-01-1336/ (accessed on 15 August 2024).